Inelastic Electron Scattering from Ni^{58}, Ni^{60}, and Ni^{62}†

M. A. DUGUAY,* C. K. BOCKELMAN, T. H. CURTIS, AND R. A. EISENSTEIN
Electron Accelerator Laboratory, Yale University, New Haven, Connecticut
(Received 23 June 1967)

Form factors are reported for the inelastic scattering of electrons from Ni^{58}, Ni^{60}, and Ni^{62} over the momentum-transfer range from 0.25 to 0.53 F^{-1}. Reduced radiative transition probabilities $B(EL)$ and transition radii R_{tr} are extracted from the data, notably for the first quadrupole and octupole states of the three isotopes. The transition radii obtained are compared to those of other nuclei.

I. INTRODUCTION

THE value of inelastic electron scattering for the study of nuclear excited states has been amply demonstrated experimentally.[1–7] Initial experiments[2–7] were carried out for the most part at energies ranging from 150 to 600 MeV, which were believed to be best suited for the study of the fine details of the transition charge density involved in the excitation of each nuclear level. Recently, however, a group of experimenters at Darmstadt,[8–15] in a series of very accurate experiments in the light elements, have demonstrated that electron scattering at relatively modest energies of 60 MeV or less is especially valuable, in that accurate values of two or more nuclear matrix elements can be reliably extracted from the form-factor measurements. In the simplest case, for example, the case of a Coulomb transition from a ground state of character 0^+ to an excited state of spin L and parity $(-1)^L$, the two matrix elements are usually quoted under the equivalent form of the reduced radiative transition probability $B(EL,0^+ \rightarrow L)$ and the transition radius R_{tr}. The first quantity, $B(EL)$, is, of course, very well known[16] and has been used for many years as an important test of theoretical nuclear wave functions. The second quantity, the transition radius, has not, however, been considered in theoretical calculations, although it clearly deserves the same status as the first.

In the work presented here we given new experimental values for the $B(EL)$'s and the transition radii for several excited states of Ni^{58}, Ni^{60}, and Ni^{62}. These new values will add to the already large list of known $B(EL)$'s and to the much smaller and lesser known list of known transition radii given by Spamer.[9] The hope is that future theoretical calculations of nuclear wave functions will be tested against *both* lists.

The form factors were analyzed with the help of the distorted-wave calculations of Onley *et al.*[17] at Duke University. In a preliminary report[18] we showed how the $B(E2)$'s for the first excited state of each isotope obtained from our electron-scattering data by means of this calculation agreed very well with the accurate Coulomb excitation measurements of Stelson and McGowan,[19] thereby providing an excellent check on this involved calculation by the Duke group.

II. APPARATUS

A. Accelerator

This experiment was performed using the Yale electron accelerator, a 75-MeV linear L-Band machine with five accelerating sections. Intense average currents, on the order of 300 μA, are available at 40 MeV with an energy spread of $\pm 5\%$; when analyzed to 0.2%, currents can be obtained in the 1.0–5.0 μA region. As the energy is increased the beam current is reduced, but the energy spread is also reduced so that the analyzed beam current remains essentially constant. When used at the highest energies, however, the analyzed current falls off considerably, and in view of this fact none of the present measurements was done at an energy higher than 65 MeV. In addition to possessing a $\pm 5\%$ spread in energy, the raw output of the machine is unstable in time and spatial position. Before electron scattering could be done, both the energy resolution and stability

† Research supported in part by the U. S. Atomic Energy Commission under Contract No. AT(30-1)2726.
* Present address: Bell Telephone Laboratories, Murray Hill, New Jersey.
[1] W. C. Barber, Ann. Rev. Nucl. Sci. **12**, 1 (1962).
[2] R. H. Hofstadter, Rev. Mod. Phys. **28**, 214 (1956); R. H. Hofstadter, Ann. Rev. Nucl. Sci. **7**, 231 (1957).
[3] J. Bellicard and P. Barreau, Nucl. Phys. **36**, 476 (1962).
[4] D. Blum, P. Barreau, and J. Bellicard, Phys. Letters **4**, 109 (1963).
[5] J. Bellicard, P. Barreau, and D. Blum, Nucl. Phys. **60**, 319 (1964).
[6] H. Crannell, R. Helm, H. Kendall, J. Oeser, and M. Yearian, Phys. Rev. **123**, 923 (1961).
[7] G. Fricke, G. R. Bishop, and D. B. Isabelle, Nucl. Phys. **67**, 187 (1965).
[8] F. Gudden and P. Strehl, Z. Physik **185**, 111 (1965).
[9] E. Spamer, Z. Physik, **191**, 24 (1966).
[10] H.-G. Clerc, K. J. Wetzel, and E. Spamer, Phys. Letters **20**, 667 (1966).
[11] H. Liesem, Z. Physik **196**, 174 (1966).
[12] O. Titze and E. Spamer, Z. Naturforsch. **21a**, 1504 (1966).
[13] M. Stroetzel and F. Gudden, Phys. Letters **22**, 485 (1966).
[14] H. Artus, P. Brix, H.-G. Clerc, F. Eigenbrod, A. Goldman, F. Gudden, E. Spamer, P. Strehl, M. Stroetzel, O. Titze, and K. J. Wetzel, in *Proceedings of the International Conference on Nuclear Physics, Gatlinburg, Tennessee, 1966* (Academic Press Inc., New York, 1967).
[15] E. Spamer and H. Artus, Z. Physik **198**, 445 (1967).
[16] J. M. Blatt and V. W. Weisskopf, *Theoretical Nuclear Physics* (John Wiley & Sons, Inc., New York, 1952); K. Alder, *et al.*, Rev. Mod. Phys. **28**, 432 (1956).
[17] T. A. Griffy, D. S. Onley, J. T. Reynolds, and L. C. Biedenharn, Phys. Rev. **128**, 883 (1962); D. S. Onley, T. A. Griffy, and J. T. Reynolds, *ibid.* **129**, 1689 (1963); D. S. Onley, J. T. Reynolds, and L. E. Wright, *ibid.* **134**, B945 (1964).
[18] M. A. Duguay, C. K. Bockelman, T. H. Curtis, and R. A. Eisenstein, Phys. Rev. Letters **17**, 28 (1966).
[19] P. H. Stelson and F. K. McGowan, Nucl. Phys. **32**, 652 (1962).

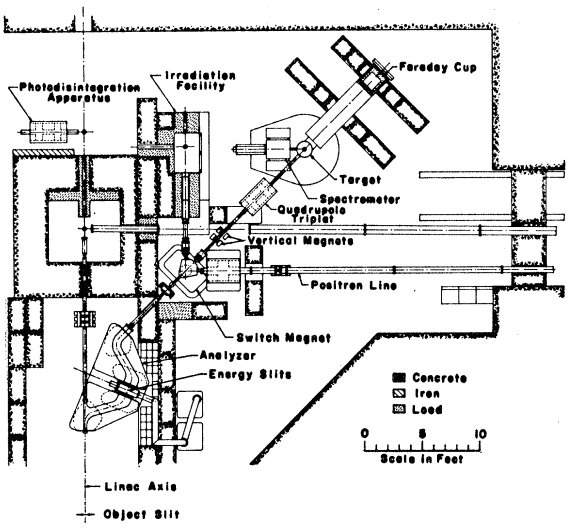

FIG. 1. Beam-handling system at the Yale electron accelerator.

of the beam were improved using conventional techniques described below. Figure 1 shows the layout of the beam-handling system as it now stands.

Beam Optics

After leaving the end of the Linac, the electron beam passes through a water-cooled aluminum slit system designed to fix the location of the beam in space. Pairs of small deflecting magnets (not shown in Fig. 1) can be used to steer maximum current through the slits. These slits form an object for a nondispersive achromatic magnetic analysis system (hereafter called the analyzer) designed by Harald Enge.[20] It is a symmetric four-pole system powered from a single supply. This system produces a 1:1 image of the object slits, with beam energy spreads controlled by the settings of the horizontal object slits and energy-defining slits placed in its symmetry plane. For most of the present experiment energy spreads of the order of 0.2% were used. The image point of the analyzer lies near the center of the switch magnet, shown also in Fig. 1. At this point, the electrons can be sent to any one of three experimental areas. For electron scattering, the beam is sent straight through the switch magnet to the target chamber of the magnetic spectrometer. The beam diverging from the analyzer image point is refocused by a quadrupole-triplet lens placed along the beam line so as to produce a demagnified image of the object slits. Thus fluctuations in the position and inclination of the beam as it leaves the accelerator do not shift the position of the target spot.

Small trimming coils on the last two poles of the analyzer are used together with small currents in the switch magnet to adjust position and direction in the horizontal plane. Vertical positioning is also needed, and it is obtained using two small magnets labeled "vertical magnets" in Fig. 1. It should be mentioned that the beam alignment is greatly facilitated by the use of two zinc-sulfide screens, each with appropriate calibration markings; one of these is placed at the image point of the analyzer and the other is at the target position within the scattering chamber. Both are viewed with close-circuit television systems, and are inserted by remote control when needed.

This system allows a very accurate determination of the location and direction of the beam at the target; in practice when all magnets are properly adjusted the beam can be focused to a round spot 1 mm in diam at the target and centered to better than 0.5 mm, with direction known to within 0.1 deg. The currents in the steering and quadrupole magnets are stabilized to 0.1% and monitored by means of a digital voltmeter.[21] During a run the beam spot never moved more than 0.5 mm; this was a determining factor in the excellent reproducibility of the data. The over-all stability of the beam-handling system was such that, after a wait of several hours required for the analyzer to reach equilibrium, the effective variation in energy of elastically scattered electrons never exceeded 0.02%.

B. Beam Collection

After passing through the target, the beam enters a "ditching" pipe 2.6-m long and 0.6-m in diam, at the end of which is a Faraday cup of standard design[22,23] used for charge collection and beam-current monitoring. The current-collection efficiency is estimated at better than 95%.[23] Stability is the crucial requirement

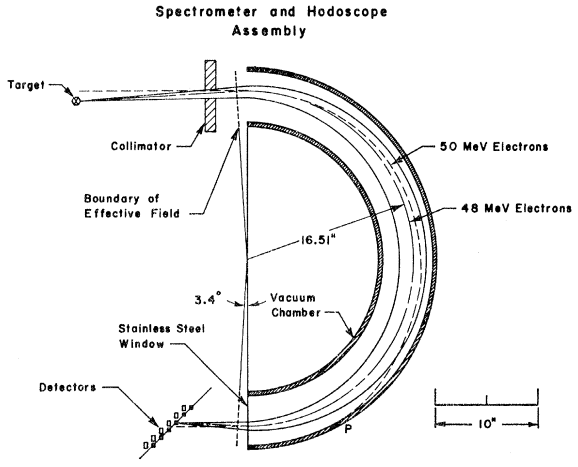

FIG. 2. Schematic cross section of the collimator, spectrometer, and hodoscope assembly.

[20] Described by E. E. Bliamptis, Rev. Sci. Instr. 35, 1521 (1964); the analysis system was built by High Voltage Engineering Corp., Burlington, Massachusetts.

[21] Magnet control and monitoring system designed by J. E. E. Baglin and constructed by J. Johnson of this laboratory.

[22] K. L. Brown and G. W. Tautfest, Rev. Sci. Instr. 27, 696 (1956).

[23] D. Isabelle, Onde électrique 421, 1 (1962).

in the present experiment because all inelastic cross sections were measured relative to elastic ones.

The beam current was monitored and integrated by an instrument of commercial design.[24] The integrator is a critical part of the experiment, so its accuracy, linearity, and reproducibility were measured carefully. The relevant numbers are absolute accuracy, 0.3–0.4%; nonlinearity, maximum of 1% at full-scale current readings; reproducibility over 24 h, 0.2%.

C. Spectrometer

The electrons scattered by the target nuclei are analyzed by an $n=\frac{1}{2}$, 180° double-focusing spectrometer[25–27] with a nominal radius of 16 in. (see Fig. 2). The device is mounted with gap vertical on a turntable which rotates about a vertical axis through the center of the target; the angular range extends from 60° to 150° with respect to the incoming beam. The target chamber has exit ports at 10° intervals over the range mentioned, so that 10 scattering angles are available. Scattered electrons are in a vacuum until they pass through a 1 mil stainless-steel window at the exit of the spectrometer.

The acceptance solid angle of the spectrometer, defined by the collimator, is 4.2×10^{-3} sr as seen from the target. The position of the focal plane was calculated using the method of Judd,[26] and trajectories of electrons of various energies and entrance angles were calculated using formulas given by Bretscher.[28]

The detector hodoscope, described in the next section, is positioned so that the small scintillators lie in the focal plane of the spectrometer, as shown in Fig. 2. A fine adjustment of hodoscope positioning was made under operating conditions to obtain best resolution. Spectrometer aberrations were found to contribute less than 0.1% to the over-all resolution.

The spectrometer magnetic field is measured with a commercial nuclear magnetic resonance (NMR)-stabilized rotating-coil fluxmeter.[29] This device is linear within 0.01%, and when originally delivered had a temperature variation of 0.3%/°C. Temperature-compensating resistors were used to replace the existing ones in a precision voltage-dividing network, and this improved the over-all stability under operating conditions to better than 0.1%/°C. When used with a long (300 ft) length of RG-55/U coaxial cable between the field probe and the control box, a phase shift between the NMR control signal and the field signal was encountered. A capacitance-compensating network corrected this.

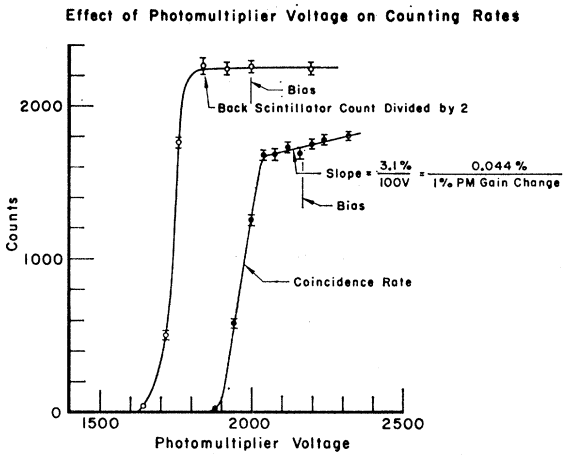

FIG. 3. The curve marked "coincidence rate" is a plot of the coincidence counting rate versus the voltage on the photomultiplier coupled to the front scintillator. A 20-nsec resolving time was used for this test. The other curve is a plot of the back scintillator singles counting rate versus the voltage applied to the back scintillator phototube. Voltages used in the actual experiment are marked "bias."

D. Detector Hodoscope

Figure 2 shows schematically the placement of the detector hodoscope. There are six detector channels, all lying in the focal plane of the spectrometer. Each channel consists of two detectors operated as a coincidence network. The detectors are Pilot B plastic scintillators[30] coupled to photomultiplier tubes[31]; signals from this arrangement are processed by a nanosecond electronics system to be described later.

The front scintillators in Fig. 2 are $2\times3\times12$ mm, except for No. 1 which is $1\times3\times12$ mm. The energy bin defined by these scintillators is 0.13% wide for Nos. 2–6, and 0.065% wide in the case of No. 1. The back scintillators are uniformly larger, measuring $3\times12\times32$ mm, and are spaced 1 cm behind the front detectors. These measurements are such that any electron from the spectrometer passing through a front scintillator will also pass through the back scintillator. The effects of multiple scattering in the front scintillator and inclination of electron paths within the acceptance solid angle of the spectrometer were taken into account.

Light collection from the back scintillators posed no problem: The scintillators were glued[32] to large parallelepiped-shape lucite light guides which transmitted the light to the photomultipliers with a measured efficiency of 40–50%. Collecting the light from the small front

[24] Elcor model No. A309A, Elcor Inc., Falls Church, Virginia.
[25] The spectrometer was loaned to the Electron Accelerator Laboratory by the U. S. Office of Naval Research through the courtesy of Professor Robert Hofstadter of Stanford University and Dr. J. Fregeau of ONR.
[26] David L. Judd, Rev. Sci. Instr. **21**, 213 (1950).
[27] C. W. Snyder, S. Rubin, W. A. Fowler, and C. C. Lauritsen, Rev. Sci. Instr. **21**, 852 (1950).
[28] M. M. Bretscher, Oak Ridge National Laboratory Report No. ORNL-2884, TID-4500 (1960), available from the Office of Technical Services, Department of Commerce, Washington 25, D. C.
[29] Fluxmeter model No. 601, J. C. Carter Co., Costa Mesa, California.
[30] Obtained from Pilot Chemicals, Inc., Watertown, Massachusetts.
[31] 56 AVP photomultipliers, Amperex Electronics Corporation.
[32] Epoxy adhesive manufactured by Carl H. Biggs Company, Santa Monica, California.

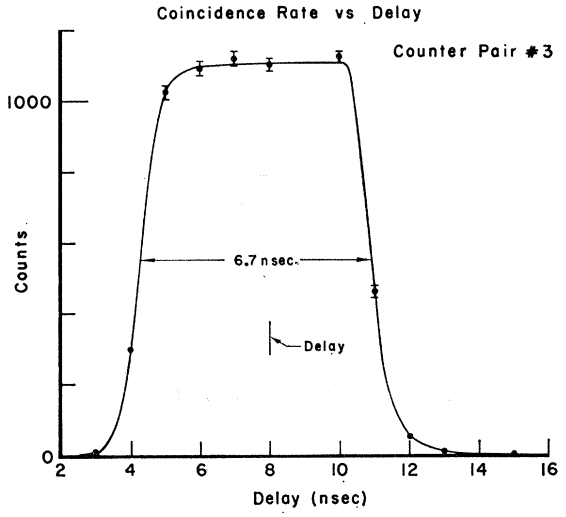

FIG. 4. The coincidence rate is plotted versus the setting of a delay box placed in one leg of the coincidence arrangement. The setting used in the experiment is marked "delay."

scintillators was more difficult because of lack of space. A compromise between light-collection efficiency and compactness was achieved by imbedding the small scintillators into small (6-mm diam) cylindrical lucite light guides. The light-collection efficiency achieved with the small scintillators varied from 20 to 30%.

The photomultipliers were wrapped with sheets of high-permeability metal to shield against the fringing field of the spectrometer. Co-Netic high-permeability metal was used on the inside and Netic metal[33] on the outside; the recommendations of Wadey[34] were followed closely. All photomultipliers showed no decrease in gain for fields corresponding to electron energies up to 65 MeV.

As is well known[35,36] in the problem of particle detection with scintillation detectors, the average number of photoelectrons released at the photocathode plays a very important role. It determines to a great extent the variation in pulse height and the time jitter of the pulses expected at the anode of the photomultiplier. The convenient method described by Colgate[35] was used to obtain an estimate of this number of minimum ionizing particles (e.g., relativistic electrons).

For the case at hand, the number of photoelectrons available was about 80 for all photomultipliers; the most sensitive photomultipliers (100 μA/lm) were selected for use with the front scintillators where the light-collection efficiency was the poorest. This resulted in a good pulse-height definition as evidenced by the very flat plateau in the curve of counting efficiency versus photomultiplier voltage (Fig. 3) and also in a small time jitter as evidenced by the very steep edges of the coincidence delay curve (Fig. 4).

The limit on the stability of the counting efficiency is set by the temperature sensitivity of the discriminators used to process the pulses from the photomultipliers. The threshold has a temperature dependence of $\approx 1\%/°C$. The slopes of the efficiency versus photomultiplier gain for the counters are all less than 0.1% per 1% change in photomultiplier gain. Under operating conditions the ambient temperature could fluctuate by $\pm 5°C$; this leads to an estimated long-term stability of 0.5% for the counting efficiencies of all counters. This figure is in agreement with the over-all reproducibility for inelastic spectra of better than 1% observed in almost all cases.

E. Electronics

The electronics is represented by a block diagram, Fig. 5. With the exception of the divider chain, all circuits were designed by Sugarman *et al.*,[37] and were constructed locally under the supervision of C.E.L. Gingell. They are ac-coupled 100 Mc/sec units with input and output impedances of 50 Ω.

The dead time of the discriminators could be set as low as 10 nsec. However, the photomultiplier pulses after traveling over 100 m of RG-9 cable were lengthened from 14 to 25 nsec. To insure a constant threshold under high counting rates, the dead time was set at 30 nsec.

The coincidence resolving time [full width at half maximum (FWHM) of the delay curve, Fig. 4] was adjusted to 7 nsec because this gave a high, stable coincidence counting rate in conjunction with a low "accidental" counting rate.

The losses for one detector due to electronic dead time can be obtained by counting the detector pulses with discriminators of two different internal dead times. Figure 5 shows the arrangement. Scaler No. 8 counts the total pulses less those lost due to the 30-nsec dead time; scaler No. 9 counts total pulses less those lost due to 60-nsec dead time. The difference in these counts is the number of counts lost due to 30 nsec of dead time. The anticoincidence circuit is used to perform this subtraction electronically; scaler 10 always read the difference and so scalers 8 and 9 could be eliminated. Since the front scintillator is so much smaller than the back, its dead-time losses are minute compared to those of the back detector. For this reason, only the dead-time losses from the back detector are monitored.

The discriminators in each detector leg are gated on only during the beam pulse. The gate generator[38] is triggered by the accelerator master trigger and is

[33] The Co-Netic and Netic metal sheets were manufactured by the Perfection Mica Company, Magnetic Shield Division, Talma, Indiana.

[34] W. G. Wadey, Rev. Sci. Instr. **27**, 910 (1956).

[35] Stirling A. Colgate, Rev. Sci. Instr. **30**, 140 (1958); **30**, (E)751 (1958).

[36] L. G. Hyman, R. M. Schwartz, and R. A. Schluter, Rev. Sci. Instr. **35**, 393 (1964).

[37] R. Sugarman, F. C. Merritt, and W. A. Higinbotham, Brookhaven National Laboratory Report No. BNL 711 (T-248) (Instruments-TID 4500), available from the Office of Technical Services, Department of Commerce, Washington, D. C.

[38] The gate generator was designed and built by Clifford Heaton.

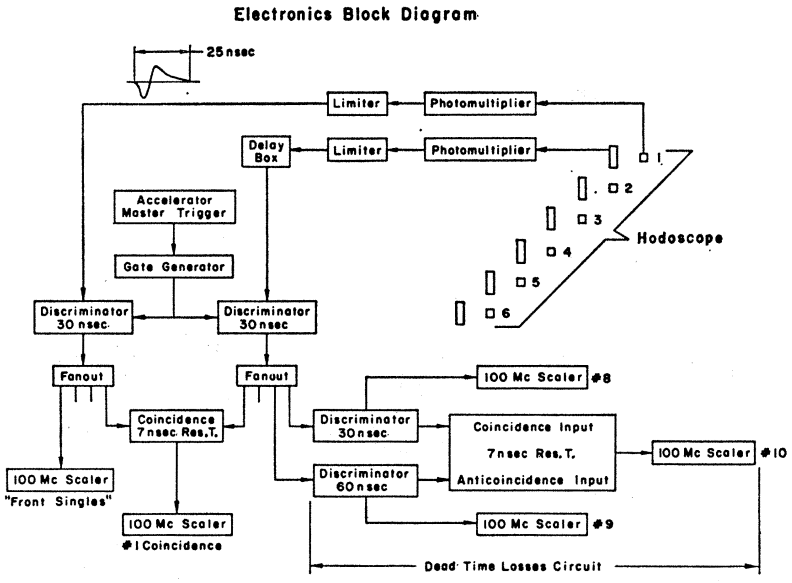

FIG. 5. Block diagram of the electronics.

adjusted so as to overlap the 4 μsec beam pulse by 3 μsec on either side.

The various pulses are counted on commercial[39] 100 Mc/sec scalers, and are read out to typewriters and tape punch with the help of locally constructed[40] digital circuits.

F. Energy Calibration

Though the incident energy was known to about 2% from the analyzer settings, it was necessary to calibrate the spectrometer in order to obtain the desired accuracy. Unfortunately, the power supply used with the spectrometer cannot furnish sufficient current to deflect α particles from the radioactive sources conventionally used for calibration. Therefore, a relation between the spectrometer fluxmeter reading and the electron energy was obtained by measuring the energy separation between C^{12} and hydrogen elastic-scattering peaks. At a fixed scattering angle, this separation is a sensitive function of the incident energy. Using the known energy difference between electrons scattered from the ground state of C^{12} and the first excited state of C^{12} at 4.4387 ± 0.0005 MeV,[41] the incident energy could be obtained. Details of the procedure are given in Ref. 42. An energy calibration good to 0.25% over the electron-energy range 40–65 MeV was obtained.

G. Instrumental Scattering

In early use of the spectrometer, it became obvious that one region of the spectrum could be obscured by instrumental scattering. This phenomenon was studied carefully by scattering electrons from a C^{12} target. Carbon-12 is ideally suited for this purpose because it has no excited states below 4.439 MeV; the inelastic spectrum between the elastic peak and this first excited state should be a smooth curve behaving roughly as $1/\Delta E$, where ΔE is the energy difference between the incident and the scattered electrons. The spectrum presented in Fig. 6 clearly shows the presence of a spurious bump superimposed on the smooth $1/\Delta E$ curve. The origin of the instrumental scattering was found to be electromagnetic showers generated by the elastically scattered electrons when they strike the outer wall of the spectrometer vacuum chamber. In Fig. 2, when the spectrometer field is adjusted so that, say, 48-MeV electrons are focused onto the counter shown, the elastically scattered electrons (at 50 MeV in this example) are hitting the spectrometer chamber over an area centered at P (only the central trajectory at 50 MeV is shown). Since inelastic peaks are usually from 100 to 10 000 times smaller than the elastic peak, it takes only a small fraction of the byproducts of the electromagnetic showers to account for the spurious bump.

The bump is strongest when point P is closest to the counters, and gradually decreases as P moves back along the spectrometer when one decreases the field. A similar bump was found *above* the elastic peak, corresponding to the same phenomenon occurring on the inner wall of the spectrometer vacuum chamber. This phenomenon would seem to have important implications on the future study of the radiative tail (or its subtraction in giant-resonance studies) with spectrometers of this type, since at any given field setting, electrons (and probably positrons also) are coming not only from the expected source but also from the walls of the spectrometer vacuum chamber.

[39] Transistor Specialties Inc., Plainview, Long Island, New York.

[40] The scaler read-out circuits were built under the direction of C. E. L. Gingell.

[41] R. Auble, A. Galonsky, and James J. Kolata, Bull. Am. Phys. Soc. **11**, 476 (1966); J. Kolata (private communication).

[42] R. A. Eisenstein, Yale Electron Accelerator Laboratory Internal Report (unpublished).

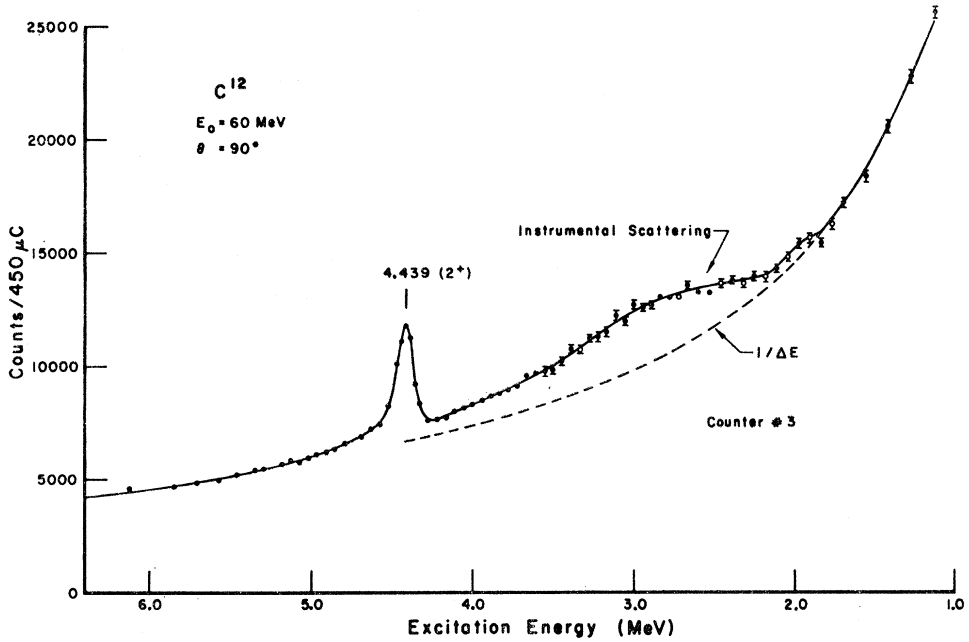

FIG. 6. Spectrum of electrons inelastically scattered from C^{12} showing the instrumental scattering in detail.

In an attempt to eliminate the spurious bump, a lead baffle 2-cm thick and 3-cm high (in the radial dimension) was inserted at point P on Fig. 2. It was successful in almost completely eliminating the bump. However, since it also seriously reduced the solid angle available to the lower counters of the hodoscope, it was not used for most of the measurements discussed here. Since the bump appears at different apparent excitation energies in different counters of the 6-channel hodoscope, it is generally possible to avoid it in any particular energy interval by proper choice of the counters used.

III. THEORY

The square of the inelastic form factor $|F_{\text{in}}|^2$ is defined as

$$|F_{\text{in}}|^2=\sigma(E_0,\theta)/\sigma_{\text{Mott}}, \quad (1)$$

where $\sigma(E_0,\theta)$ is the absolute differential cross section for the inelastic process measured at incident electron energy E_0 and where σ_{Mott}, the so-called Mott cross section, is defined as

$$\sigma_{\text{Mott}}=\left(\frac{Ze^2}{2E_0}\right)^2\frac{\cos^2\frac{1}{2}\theta}{\sin^4\frac{1}{2}\theta}. \quad (2)$$

The Mott cross section describes the elastic scattering of electrons by a point nucleus of spin zero in the Born approximation. It is used only as a unit here, so to speak, and does not imply that any approximation is made in the analysis.

A. Born Approximation

Before going into the details of the distorted-wave analysis, it is very useful to write down the expression for the form factor F_{in} in the Born approximation in order to present the essentials of the inelastic process. We wish to emphasize that the results described in Sec. IV were *not* analyzed in the Born approximation. The latter is used only as a valuable aid in visualizing the important elements of the inelastic-scattering process.

In the excitation of a nuclear state of spin $J_f=L$ from a 0^+ ground state, as was the case here, only the Lth multipole of the electron field contributes to the interaction and the inelastic form factor, neglecting the finite mass of the electron and the finite energy loss, is equal to

$$|F_{\text{in}}(q,\theta)|^2=|F_{CL}(q)|^2+(\tfrac{1}{2}+\tan^2\tfrac{1}{2}\theta)|F_{EL,ML}(q)|^2. \quad (3)$$

In this equation $q=|\mathbf{p}_i-\mathbf{p}_f|$, the three-momentum transfer of the electron; $|F_{CL}|$ is the part of the total form factor due to the Coulomb or longitudinal part of the interaction; and $|F_{EL,ML}|$ is due to the transverse electric part (F_{EL}) of the interaction if the parity of the final state is $(-1)^L$, or to the transverse magnetic part (F_{ML}) of the interaction if the final-state parity is $(-1)^{L+1}$.

In the present experiment we were concerned mainly with collective states, for which theoretical estimates predict very small transverse form factors. The conventional detection of transverse effects is obtained by comparing form factors measured at forward and backward angles, using incident energies adjusted to produce the same momentum transfer. Our measurements, through the back-angle enhancement expected from Eq. (3), would indicate that transverse contributions are less than 10% for all levels measured (excluding the Ni^{62} 2^+ state, for which no 150° measurements were taken). However, since Coulomb distortion of the elec-

tron waves, neglected in Eq. (3), is not negligible, further checks were made using the liquid-drop model in distorted-wave calculation to be described later. These calculations predict transverse contributions of less than 1% of the Coulomb form factor in our range of momentum transfer. We shall, therefore, for purposes of the present discussion, neglect transverse form factors and write

$$|F_{\text{in}}|^2=|F_{CL}|^2. \tag{4}$$

In the Born approximation the form factor squared $|F_{CL}|^2$ for a transition from the ground state of spin J_i to a state of spin J_f is[43]

$$|F_{CL}|^2=\frac{4\pi}{Z^2}\sum_{L=0}^{\infty}\frac{|\langle J_f\|\hat{M}_L^{\text{Coul}}(q)\|J_i\rangle|^2}{(2J_i+1)}, \tag{5}$$

where

$$\hat{M}_{LM}^{\text{Coul}}(q)=\int j_L(qr)Y_{LM}(\Omega)\hat{\rho}d^3r. \tag{6}$$

Here j_L is the spherical Bessel function of order L and $\hat{\rho}$ is the nuclear charge-density operator. The reduced matrix element is defined by the Wigner-Eckart theorem[44]

$$\langle J_fM_f|\hat{M}_{LM}|J_iM_i\rangle=(-)^{J_f-M_f}\begin{pmatrix}J_f & L & J_i\\ -M_f & M & M_i\end{pmatrix}\langle J_f\|\hat{M}_L\|J_i\rangle. \tag{7}$$

Thus, inserting (6) in (7), we get

$$(-)^{J_f-M_f}\begin{pmatrix}J_f & L & J_i\\ -M_f & M & M_i\end{pmatrix}\int j_L(qr)Y_{LM}\langle J_f\|\hat{\rho}\|J_i\rangle d^3r=\int j_L(qr)Y_{LM}\rho_{fi}(\mathbf{r})d^3r, \tag{8}$$

with

$$\rho_{fi}(\mathbf{r})=\langle J_fM_f|\hat{\rho}|J_iM_i\rangle. \tag{9}$$

Equation (9) defines the transition charge density $\rho_{fi}(\mathbf{r})$. For $J_i=0^+$ and $J_f=L$ we have for (5)

$$|F_{CL}|^2=\frac{4\pi}{Z^2}(2L+1)\left[\int j_L(qr)Y_{LM}\rho_{fi}(\mathbf{r})d^3r\right]^2. \tag{10}$$

A common form for the charge density operator is

$$\hat{\rho}=\sum_{i=1}^{A}|e|\,\epsilon_i\delta(\mathbf{r}-\mathbf{r}_i), \tag{11}$$

with $\epsilon_i=1$ for protons and $\epsilon_i=0$ for neutrons. A is the number of nucleons and $\mathbf{r}_i$ is the coordinate of the ith nucleon. In the present treatment, a form for the matrix element $\rho_{fi}(\mathbf{r})$ is chosen as

$$\rho_{fi}(\mathbf{r})=\rho(r)Y_{LM}^*(\Omega), \tag{12}$$

about which more will be said later.

[43] T. deForest, Jr., and J. D. Walecka, Advan. Phys. **15**, 1 (1966).

[44] A. deShalit and I. Talmi, *Nuclear Shell Theory* (Academic Press, Inc., New York, 1963).

If we now expand the Bessel function in (10), we have

$$|F_{CL}|^2=\frac{4\pi q^{2L}(2L+1)}{Z^2[(2L+1)!!]^2}\left[I_L-\frac{q^2}{2(2L+3)}I_{L+2}+\frac{q^4}{8(2L+3)(2L+5)}I_{L+4}+\cdots\right]^2, \tag{13}$$

where

$$I_k=\int r^k\rho_{fi}(\mathbf{r})Y_{LM}d^3r. \tag{14}$$

The reduced transition probability for electromagnetic transitions $B(EL,J_i\to J_f)$ is defined as[44]

$$B(EL,J_i\to J_f)=\frac{1}{(2J_i+1)}|\langle J_f\|\int r^LY_{LM}\hat{\rho}d^3r\|J_i\rangle|^2. \tag{15}$$

For the case $0\to L$, we use the Wigner-Eckart theorem, and find

$$B(EL,0^+\to L)=(2L+1)\left[\int r^LY_{LM}\rho_{fi}(\mathbf{r})d^3r\right]^2=(2L+1)I_L^2. \tag{16}$$

Thus, (13) can be rewritten in the form

$$\frac{|F_{CL}|^2}{q^{2L}}=\frac{4\pi B(EL)}{Z^2[(2L+1)!!]^2}\left[1-\frac{q^2}{2(2L+3)}R_{\text{tr}}^2+\cdots\right]^2. \tag{17}$$

Here R_{tr} is the transition radius defined as

$$R_{\text{tr}}^2=I_{L+2}/I_L. \tag{18}$$

Equation (13), or equivalently, Eq. (17), may be construed to define the aim of inelastic electron-scattering measurements. This aim is to extract, from accurate measurements of the form factor $|F_{CL}|$ over a certain momentum-transfer range, values of moments of transition charge densities I_k for comparison with theoretical nuclear models.

For small qr the first two terms of the expansion, Eq. (17), strongly dominate so that extraction of $B(EL)$ and R_{tr} is straightforward, *in the Born approximation*. In the light elements, where the latter applies, the Darmstadt experimenters could use it successfully. As long as the contribution of higher terms is negligible it is not necessary to make any assumption about the shape of the transition charge density. In such a case the extraction of $B(EL)$ and R_{tr} can be termed "model-independent."[45]

B. Distorted-Wave Calculations

In the distorted-wave analysis, the relation between form factors and matrix elements is much more complicated, so much so, in fact, that it can only be obtained

[45] The third term can make a 20% contribution to $|F_{CL}|^2$ for Ni at the largest q^2 available to 60-MeV electrons. The Darmstadt experimenters made the mild assumption that the third term, $(I_{L+4}/I_L)\approx R_{\text{tr}}^4$. This assumes that the transition charge density is concentrated near the surface of the nucleus.

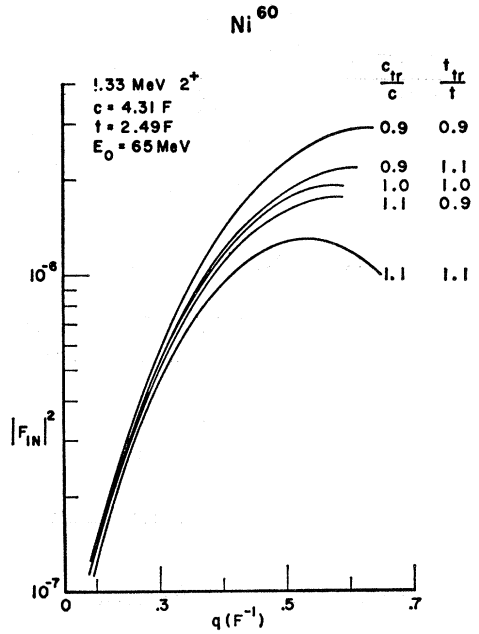

FIG. 7. Theoretical $|F_{\text{in}}|^2$ versus q for the Ni^{60} 1.332-MeV 2^+ level. The parameters c and t are the half-density radius and skin thickness of the ground-state Eq. (19); c_{tr} and t_{tr} are the parameters of the transition charge density, Eq. (20). The incident energy is 65 MeV. The curves are calculated using code GBROW, with $B(E2)$ set equal to $1(e^2F^4)$. Also shown are the effects of 10% variations in c_{tr} and t_{tr}.

by lengthy numerical computations. However, we retain from the Born approximation two aspects of inelastic electron scattering which are expected to persist in the distorted-wave case;

(a) The value of $|F_{CL}|^2/q^{2L}$ extrapolated to $q=0$ must be directly related to the value of $B(EL)$, and the initial rate at which this quantity falls off as q^2 increases should be also directly related to the value of R_{tr}^2.

(b) A certain amount of "model independence" should persist, meaning that different transition charge densities will give nearly identical form factors over the low-q range provided that the values of $B(EL)$ and R_{tr}^2 corresponding to these transition charge densities are equal. We shall see in Sec. VI C how actual calculations corroborate this expectation.

The experimental results were analyzed using the Duke distorted-wave computer program,[17] known as Code GBROW.[46] The essential difference between this calculation and the Born-approximation approach described above is the replacement of plane electron waves by sums of partial waves obtained by numerical integration of the Dirac equation for the Coulomb field of a nucleus of finite size. In order to calculate the cross section for inelastic scattering to a specific nuclear level, it is necessary to insert values of the ground-state charge distribution, the transition-charge density (which gives rise to the longitudinal term), and the transition current and magnetization densities (which give rise to the transverse terms).

In the present calculation, the ground-state charge density was taken as a Fermi distribution,

$$\rho(r)=\rho_0\left[1+\exp\left(\frac{r-c}{t/4.4}\right)\right]^{-1}, \tag{19}$$

where $c=c_0A^{1/3}$ determines the radius and t determines the 90–10% skin thickness. Because the particular states studied were expected to be collective in nature, following Onley *et al.*,[17] the transition charge density was taken as

$$\rho_{fi}(\mathbf{r})=\rho_{\text{tr}}(r)Y_{LM}(\hat{r})e^{i\omega t},$$

with

$$\rho_{\text{tr}}(r)=N_Lr^{L-1}\frac{d}{dr}\left[1+\exp\left(\frac{r-c_{\text{tr}}}{t_{\text{tr}}/4.4}\right)\right]^{-1}, \tag{20}$$

where $c_{\text{tr}}=c_{0\text{tr}}A^{1/3}$ determines the radius and t_{tr} defines the skin thickness of the radial part of the transition charge density ρ_{tr}. N_L is a normalization constant which adjusts the strength of the transition.

This form of $\rho_{\text{tr}}(r)$, with $c_{\text{tr}}=c$, and $t_{\text{tr}}=t$, was first introduced by Tassie,[47] who studied the hydrodynamical nuclear model where one-phonon collective excitations are treated as vibrations of a liquid drop having a charge distribution of the shape described in the argument of the radial derivative (the Fermi shape here). The liquid is assumed to be irrotational and incom-

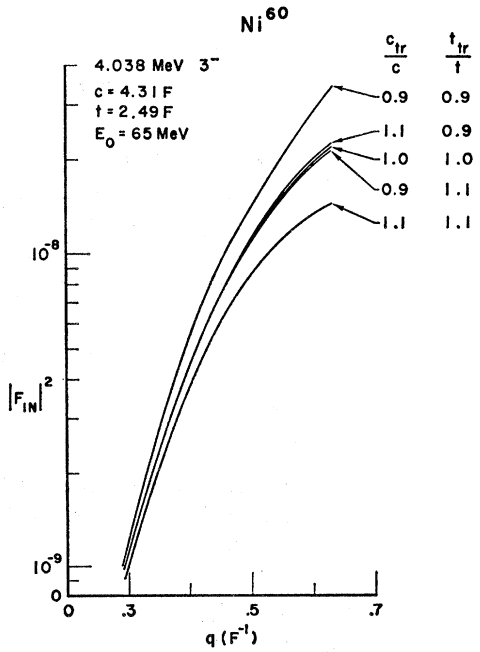

FIG. 8. Theoretical $|F_{\text{in}}|^2$ versus q for the Ni^{60} 4.038-MeV 3^- level, with $B(E3)$ set equal to $1(e^2F^6)$. All other parameters are as in Fig. 7.

[46] J. Ziegler, *The Calculation of Inelastic Electron Scattering by Nuclei*, U. S. Atomic Energy Commission, Division of Technical Information, National Bureau of Standards, U. S. Dept of Commerce, Springfield, Virginia 22151.

[47] L. J. Tassie, Australian J. Phys. 9, 407 (1956).

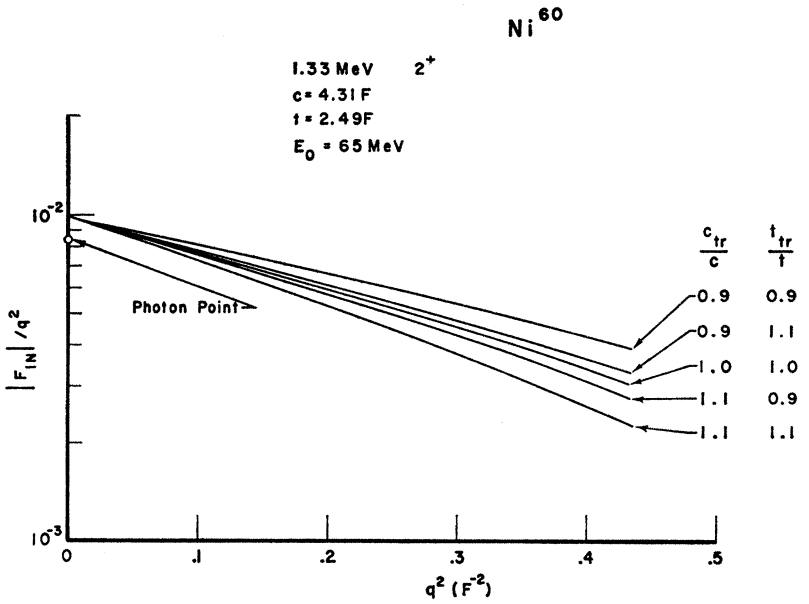

FIG. 9. Theoretical $|F_{in}|/q^2$ versus q^2, drawn on a semilog plot for the Ni^{60} 1.332-MeV 2^+ level. The calculations are identical with those of Fig. 7. The "photon point" is the intercept of the Born-approximation calculation when plotted as $|F_{in}|/q^2$ versus q^2, and is explained in the text. The various curves show the effect of the 10% variations in c_{tr} and t_{tr}.

pressible. In this model the contribution of the transverse term is small.

In Figs. 7 and 8 the calculated variation of $|F_{in}|^2$ with momentum transfer q are displayed for the Ni^{60} 2^+ state at 1.332 MeV and the 3^- state at 4.038 MeV, using Eqs. (19) and (20) for the ground state and transition charge densities, respectively. Also shown are the effects of 10% variations in c_{tr} and t_{tr}. The normalization of these curves is such that the reduced transition probability $B(EL)$ is equal to 1.0 e^2 $F^{2L}=(197.3)^{-2L}$ e^2 MeV^{-2L}. To perform this normalization, Code GBROW calculates $B(EL)$ according to Eq. (16) and then divides the final distorted wave $|F_{in}|^2$ by this calculated value.

By comparing the measured form factors to the theoretical curves, one attempts to define the transition charge density as closely as the experiment permits. To facilitate this comparison it is useful to recall the earlier discussion. Equation (17) shows that in the Born approximation, when higher terms can be neglected, a plot of $|F_{CL}|/q^L$ against q^2 is a straight line with intercept measuring $B(EL)$ and slope measuring R_{tr}. It is found empirically that when the distorted wave results are plotted in the form $\log|F_{in}|/q^L$ versus q^2, a rather similar plot is obtained. In Figs. 9 and 10, results of the distorted-wave calculations of the previous paragraph are replotted in this form. It is seen that nearly straight lines are produced for the momentum range studied; at higher q the curvature is more evident.

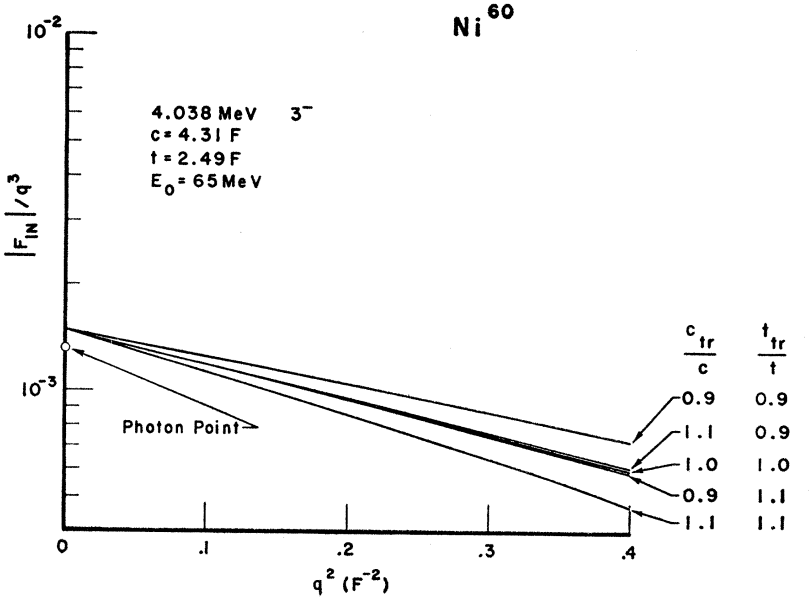

FIG. 10. Theoretical $|F_{in}|/q^3$ versus q^2, drawn on a semilog plot for the Ni^{60} 4.038-MeV 3^- level. The calculations are identical with those of Fig. 8. The "photon point" is the intercept of the Born-approximation calculation when plotted as $|F_{in}|/q^3$ versus q^2 and is explained in the text. The various curves show the effect of the 10% variations in c_{tr} and t_{tr}.

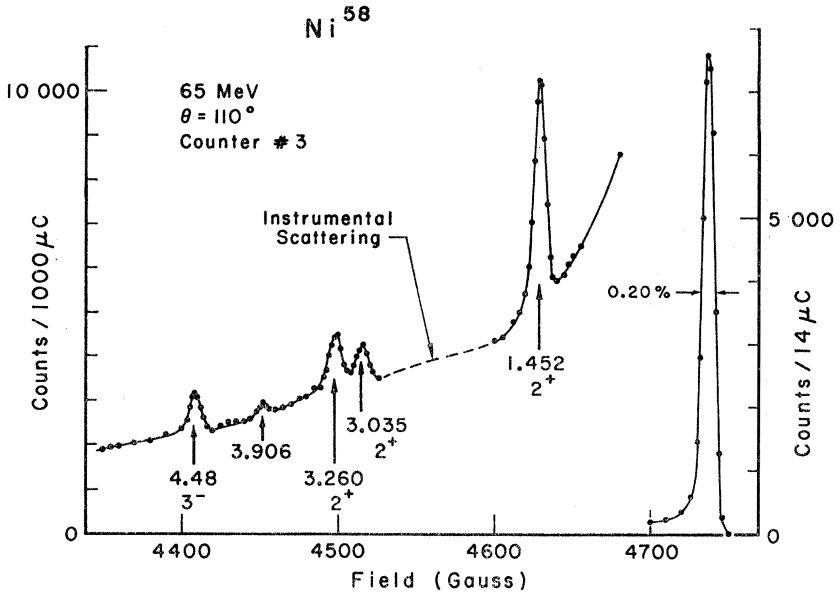

FIG. 11. Ni^{58} spectrum observed in counter telescope No. 3. The incident energy is 65 MeV and the laboratory scattering angle is 110°. The peak on the extreme right of the figure is the elastic-scattering peak.

The lines converge to a common intercept at $q=0$ as a result of the normalization of the $B(EL)$. The effect of the Coulomb distortion may be noted by observing the displacement between this intercept and the quantity $[4\pi B(EL)]^{1/2}/Z(2L+1)!!$ (the "photon point") marked on the $q=0$ axis. According to Eq. (17) this point is the intercept of a Born-approximation curve calculated for the same transition charge density. The slopes of the curves of Figs. 9 and 10 are parameter-dependent. These slopes, which must be related to the transition radii R_{tr} defined in Eq. (18), are fixed by the experimental data.

Such logarithmic plots were found useful in studying the effects of parameter variation. It is seen that increasing either the radius or the skin thickness of the transition charge density causes the lines to slope down more rapidly. It is also clear that there exist pairs of values for c_{tr} and t_{tr} which would produce equivalent results. While testing the effects of parameter variation, it was observed that the *change* in form factor resulting from a parameter change in the distorted-wave calculation was closely equal to the *change* in form factor calculated in the Born approximation.

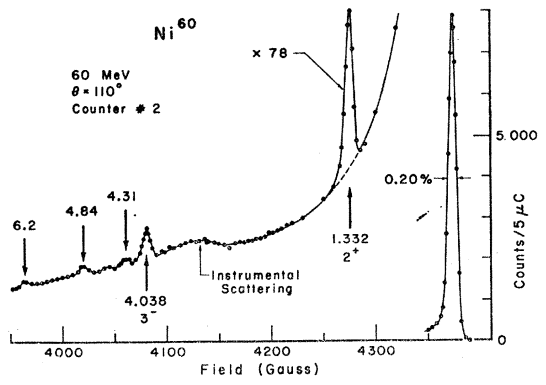

FIG. 12. Ni^{60} spectrum as observed in counter telescope No. 3. The incident energy is 60 MeV and the laboratory scattering angle is 110°.

IV. DATA

Three foils 0.001-in. thick of metallic Ni enriched to 95% in $Ni^{58,60,62}$, respectively, were used as targets. Spectra of electrons scattered from these targets are presented in Figs. 11–13. Comparing with the level schemes obtained from a variety of other experiments,[48–52] Fig. 14, it is clear that only a few of the existing states have been observed in the present measurement. The transitions observed are those indicated by vertical arrows in Fig. 14. Form factors were studied at a number of incident energies in the range 45–65 MeV, and at angles between 70° and 150°.

In the present experiment, no attempt has been made to measure absolute cross sections; rather the ratio R of inelastic to elastic scattering was measured, and the absolute inelastic cross sections were calculated using absolute elastic cross sections derived from the Stanford measurement of the elastic cross section for Ni^{58} at 183 MeV.[53] The Stanford experimenters found that their data could be fitted by a Fermi charge distribution of the form of Eq. (19), with $c=4.25\pm0.09$ F and

[48] *Nuclear Data Sheets*, compiled by K. Way *et al.* (U. S. Government Printing Office, National Academy of Sciences–National Research Council, Washington 25, D. C.).
[49] Kuzuhisa Matsuda, Nucl. Phys. **33**, 536 (1962).
[50] L. W. Swenson and R. K. Mohindra, Phys. Rev. **150**, 877 (1966).
[51] P. F. Hinrichsen, G. T. Wood, and S. M. Shafroth, Nucl. Phys. **81**, 449 (1966).
[52] E. R. Cosman, C. H. Paris, A. Sperduto, and H. Enge, Phys. Rev. **142**, 673 (1966).
[53] B. Hahn, R. Hofstadter, and D. G. Ravenhall, Phys. Rev. **105**, 1353 (1957).

$t=2.49\pm0.25$ F. Lacking absolute values for the other Ni isotopes, it has been assumed that $c=c_0A^{1/3}$, with $c_0=1.10\pm0.02$ F for all Ni isotopes studied here. The skin thickness t was held constant at 2.49 F.

Once values of c and t were chosen, absolute elastic cross sections were calculated using the phase-shift computer code of Rawitscher and Fischer.[54] This code was checked against similar codes from Saclay[55] and M.I.T.[56]; all three gave answers identical within 0.1% over the range of energies and angles used in the present work.

The inelastic form factor was then obtained by using the relation

$$|F_{\text{in}}(E_0,\theta)|^2=\frac{\sigma_{\text{inel}}}{\sigma_{\text{el}}}\frac{\sigma_{\text{el}}}{\sigma_{\text{Mott}}}=R|F_{\text{el}}|^2, \quad (21)$$

where σ_{Mott} is defined by Eq. (2).

In electron-scattering experiments it is necessary to consider radiative corrections to the measured peaks;

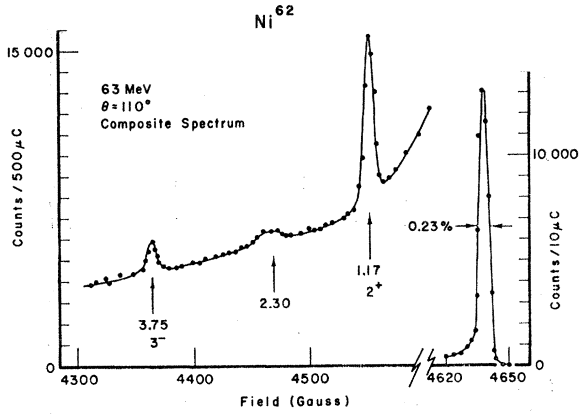

FIG. 13. Ni^{62} composite spectrum. Various portions of this spectrum were observed in different counter telescopes, and then combined on a common scale. The incident energy is 63 MeV and the laboratory scattering angle is 110°.

but these corrections apply to both elastic and inelastic peaks,[57] and are equal to within 1% for the excitation range here studied. Therefore, they do not appreciably affect the ratio of cross sections and were neglected, as were the bremsstrahlung corrections.[2]

Since the inelastic peaks were expected to have the same shape as the elastic peaks, the ratio R of the inelastic to the elastic cross section was taken as equal to the ratio of inelastic- to elastic-peak heights. This ratio was obtained by use of a computer program which performed a least-squares matching of the inelastic to the elastic peak, the data being corrected for the variation

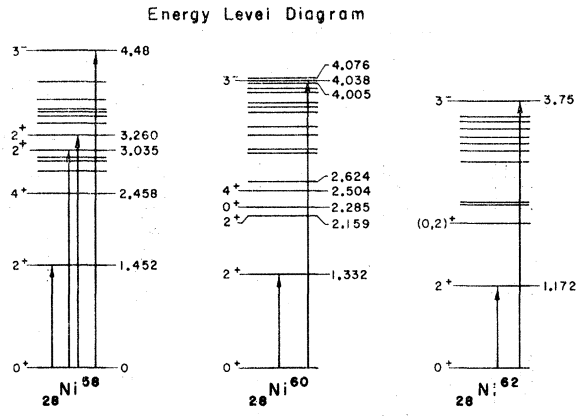

FIG. 14. Nuclear level schemes for $Ni^{58,60,62}$ in units of MeV. See Refs. 48–52.

in spectrometer dispersion. The radiative tail on which the inelastic peaks ride was fitted by an expression of the type $A/\Delta E+B/(\Delta E)^2$, where ΔE is the energy difference between the center of the elastic peak and the point on the inelastic spectrum. The parameters A and B were determined by least-squares fitting to the observed smooth background, thereby avoiding the difficult problem of the calculation of the radiative tail. Such a procedure is useful when a smooth tail can be clearly distinguished on either side of the inelastic peaks; it has been used with success in previous electron-scattering experiments at Darmstadt.[11] Some typical fits to the data are shown in Figs. 15–18.

The form factors obtained for each of the eight states studied are entered in Table I. Listed in this table are values of the incident electron energy E_0, the scattering angle θ, the three-momentum transfers q_{el} and, q for the elastic and inelastic processes, respectively, the square of the elastic form factor $|F_{\text{el}}|^2$ computed with the code of Rawitscher and Fischer,[54] the ratio R

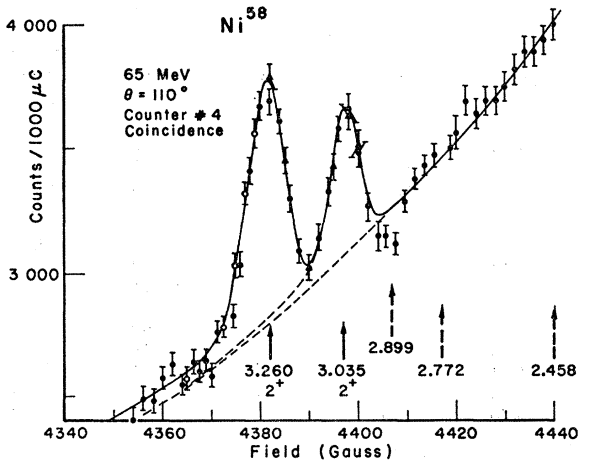

FIG. 15. Portion of the observed inelastic spectrum of Ni^{58} showing the 2^+ states at 3.035 and 3.260 MeV in counter telescope No. 4. Also indicated are the calculated positions of peaks corresponding to other known levels in Ni^{58}.

[54] C. R. Fischer and G. H. Rawitscher, Phys. Rev. **135**, B377 (1964).
[55] J. Bellicard (private communication).
[56] R. Verdier (private communication).
[57] D. R. Yennie, S. C. Frautschi, and H. Suura, Ann. Phys. (N. Y.) **13**, 379 (1961).

TABLE. I. Data and results.

E_0 (MeV)	θ (deg)	q_{el} (F^{-1})	q (F^{-1})	$\lvert F_{el}\rvert^2$	10^4R	Sta. error (%)	χ^2/N	$10^4\lvert F_{in}\rvert^2$	$10^4\lvert F_{in}\rvert^2$ "65 MeV"
Ni^{58}									
				2^+ level at 1.45 MeV					
45.12	70	0.263	0.258	0.791	2.77	8	1.0	2.19	2.04
45.21	90	0.324	0.319	0.633	6.50	7	1.7	4.11	3.82
44.21	110	0.367	0.361	0.521	10.50	7	1.2	5.47	5.11
45.26	130	0.416	0.409	0.399	21.40	5	1.3	8.54	8.02
54.80	110	0.455	0.449	0.309	32.20	3	1.0	9.95	9.72
53.92	150	0.528	0.521	0.178	67.70	10	0.9	12.05	11.86
64.27	110	0.534	0.528	0.173	72.00	3	1.0	12.44	12.44
				2^+ level at 3.30 MeV					
45.21	90	0.324	0.313	0.633	0.70	15	1.2	0.44	0.41
54.80	110	0.455	0.443	0.309	3.77	6	2.2	1.17	1.14
59.91	110	0.498	0.485	0.229	7.00	6	2.0	1.60	1.58
54.41	150	0.533	0.518	0.171	10.00	20	1.0	1.71	1.68
64.28	110	0.534	0.521	0.173	8.30	7	1.4	1.43	1.43
				2^+ level at 3.26 MeV					
45.21	90	0.324	0.312	0.633	1.26	12	1.4	0.80	0.74
41.95	130	0.386	0.370	0.477	3.87	20	1.5	1.85	1.68
54.80	110	0.455	0.442	0.309	6.62	3	1.9	2.05	2.00
59.91	110	0.498	0.484	0.229	16.50	4	2.2	3.78	3.74
54.41	150	0.533	0.517	0.171	18.20	15	0.4	3.11	3.06
64.27	110	0.534	0.520	0.173	15.70	3	1.1	2.71	2.71
				3^- level at 4.48 MeV					
54.80	110	0.455	0.436	0.309	4.10	4	1.5	1.27	1.22
59.91	110	0.498	0.479	0.229	7.93	5	1.8	1.82	1.79
54.41	150	0.533	0.511	0.171	15.60	14	0.8	2.66	2.53
64.28	110	0.534	0.515	0.173	13.70	7	1.1	2.37	2.37
Ni^{60}									
				2^+ level at 1.33 MeV					
45.12	70	0.263	0.259	0.785	3.25	5	2.1	2.55	2.37
45.18	90	0.324	0.319	0.625	9.80	3	1.5	6.13	5.70
45.19	110	0.376	0.370	0.490	16.20	3	2.3	7.94	7.41
45.25	130	0.416	0.410	0.390	27.90	6	0.8	10.89	10.24
59.95	90	0.430	0.425	0.355	31.30	3	3.5	11.12	10.96
54.80	110	0.455	0.450	0.301	42.20	2	1.0	12.69	12.40
59.94	90	0.498	0.493	0.221	67.50	3	0.9	14.93	14.79
54.38	150	0.533	0.526	0.164	96.40	12	2.5	15.84	15.60
64.23	110	0.534	0.528	0.167	98.90	7	4.0	16.48	16.48
				3^- level at 4.03 MeV					
59.94	90	0.430	0.415	0.355	3.92	10	0.6	1.39	1.37
54.80	110	0.455	0.438	0.301	6.83	4	0.9	2.05	1.98
59.94	110	0.498	0.481	0.221	12.40	4	1.4	2.74	2.70
63.72	110	0.529	0.512	0.173	20.60	8	1.2	3.56	3.56
54.38	150	0.533	0.513	0.164	22.00	5	1.0	3.61	3.43
Ni^{62}									
				2^+ level at 1.17 MeV					
45.10	70	0.263	0.259	0.778	3.28	8	1.0	2.55	2.37
45.18	90	0.324	0.320	0.617	9.58	10	1.0	5.91	5.50
45.17	110	0.375	0.371	0.482	18.30	5	1.3	8.82	8.22
45.28	130	0.416	0.411	0.381	28.40	7	1.0	10.82	10.17
54.88	110	0.456	0.451	0.291	45.60	2	2.5	13.28	12.97
56.10	120	0.493	0.488	0.222	63.70	4	0.8	14.12	13.84
64.24	110	0.534	0.529	0.160	104.30	2	1.9	16.68	16.68
				3^- level at 3.75 MeV					
58.42	70	0.340	0.329	0.562	1.06	17	0.5	0.60	0.59
56.24	70	0.327	0.316	0.596	0.77	21	0.5	0.46	0.45
60.27	70	0.351	0.340	0.534	0.96	9	4.2	0.51	0.50
56.25	90	0.404	0.390	0.405	1.68	17	1.3	0.68	0.66
60.25	90	0.432	0.419	0.340	2.98	4	6.3	1.01	1.00
56.24	110	0.467	0.451	0.267	5.52	10	1.3	1.47	1.44
56.10	120	0.493	0.476	0.220	9.50	14	2.0	2.09	2.02
60.26	150	0.590	0.572	0.089	43.00	5	1.2	3.84	3.71

of the inelastic- to elastic-peak height, the statistical error on R, the ratio of the conventional χ^2 to the number of degrees of freedom N (as a measure of goodness of fit in determining R), the inelastic form factor squared $|F_{in}|^2$, and the value of $|F_{in}|^2$ normalized to 65-MeV bombarding energy (the significance of this small correction will be explained later). The values of χ^2/N is seldom much larger than unity, indicating that the fits

were generally good. The few cases of large χ^2/N are attributed to slow drifts in the system of magnets described in Sec. II.

V. ANALYSIS

In order to obtain the nuclear matrix elements, the data were analyzed using the distorted-wave formalism of Onley *et al.*,[17] as expressed in Code GBROW.[46] Calculation of a single angular distribution when the effects of finite energy loss are included requires of the order of 10 min on the Yale computer center IBM 7090-7094 direct-coupled system, although shorter forms of the calculation[46] can be quite accurate in appropriate cases. In order to reduce computing expense, a series of com-

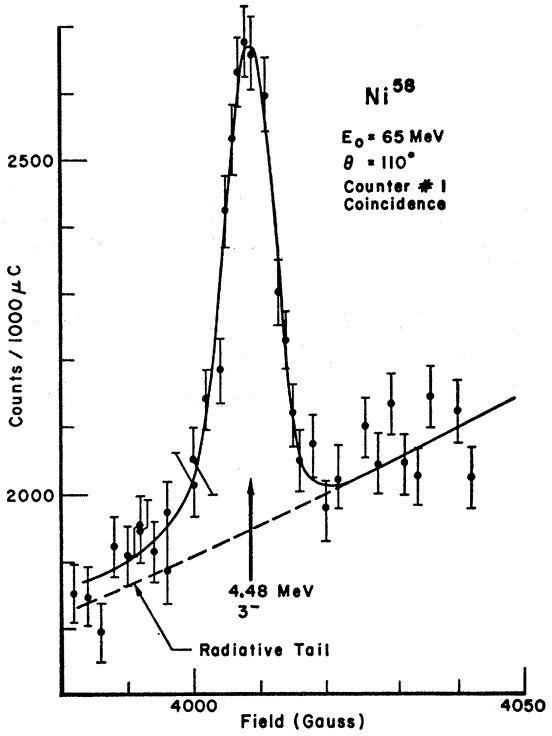

FIG. 16. The 4.48-MeV 3^- level in Ni^{58} as observed in counter telescope No. 1.

putations for the first 2^+ and 3^- states of Ni^{60} were made for bombarding energies between 40 and 75 MeV. These results were used to provide correction factors to renormalize all data to 65 MeV; the dependence of these correction factors on excitation energy and the specific parameters of the charge distribution used is weak. Further, the correction factors for individual points never exceed 8% and are usually less than 5%, as may be seen by comparing the last two columns in Table I. The form factors, normalized in this manner to 65-MeV bombarding energy, are listed in column 10 of Table I and displayed in Figs. 19–26.

The solid curves in Figs. 19–26 represent the fits to the data using Code GBROW to compute theoretical form factors. Ground-state charge densities of the form of Eq. (19), with $c=1.10A^{1/3}$ F and $t=2.49$ F were used,

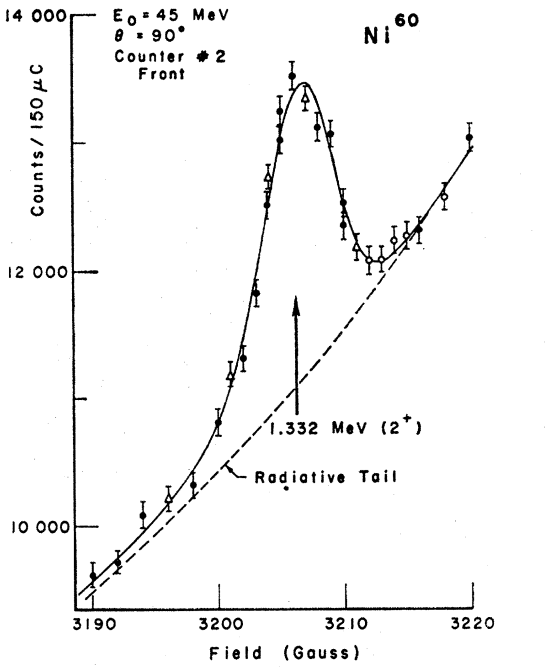

FIG. 17. The 1.332-MeV 2^+ level in Ni^{60} as observed in the front scintillator of counter telescope No. 2.

together with the hydrodynamical model employing transition charge densities of the form of Eq. (20), with $c_{tr}=c$ and $t_{tr}=t$. The code was run in a mode whereby the finite mass of the electron and the finite energy loss were taken into account. The code produces a plot of $|F_{in}|^2$ versus angle, normalized to a radiative transition

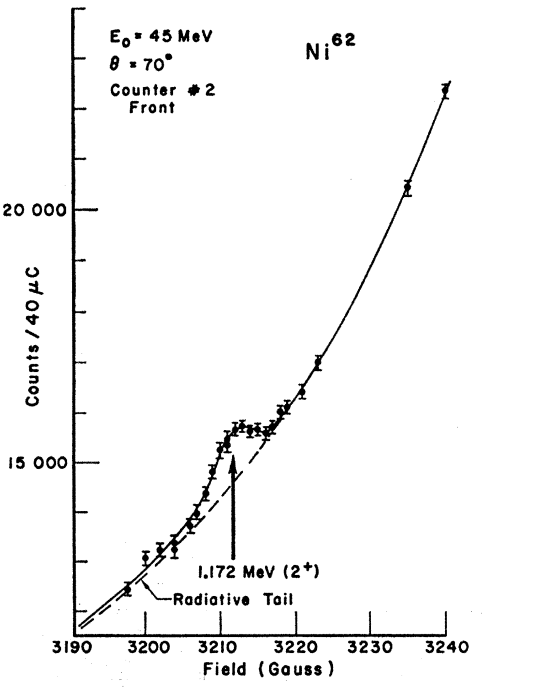

FIG. 18. The 1.172-MeV 2^+ level in Ni^{62} as observed in the front scintillator of counter telescope No. 2.

TABLE II. Reduced radiative transition probabilities and transition radii.

	Excitation energy (MeV)	$B(E2,0^+ \to 2^+)$ (e^2F^4)	$\frac{B(E2,0^+ \to 2^+)}{B(E2,0^+ \to 2^+)_{sp}}$	β_2	R_{tr} (F)
E2 Transitions[a]					
Ni^{58}	1.452	657± 11	10	0.177±0.003	5.51
	3.034	83± 3	1	0.063±0.002	5.51
	3.26	153± 15	2	0.085±0.008	5.51
Ni^{60}	1.330	845± 9	12	0.197±0.002	5.55
Ni^{62}	1.172	877± 11	12	0.197±0.001	5.59
E3 Transitions[a]					
	Excitation energy (MeV)	$B(E3,0^+ \to 3^-)$ (e^2F^6)	$\frac{B(E3,0^+ \to 3^-)}{B(E3,0^+ \to 3^-)_{sp}}$	β_3	R_{tr} (F)
Ni^{58}	4.480	18 600±520	13	0.203±0.005	6.05
Ni^{60}	4.038	28 100±640	19	0.241±0.006	6.09
Ni^{62}	3.75	20 100±540	13	0.197±0.005	6.11

[a] The errors quoted for $B(EL)$ assume the liquid-drop model for the transition charge density and are purely statistical in nature. The estimate of error from dependence on the parameters of this charge density are ±15% for both $B(EL)$ and R_{tr}. See text.

probability of unity. The curve was matched to the data by a least-squares fit, thereby determining the experimental $B(EL)$ and the normalization constant N_L in Eq. (20); the transition radius R_{tr} was computed by carrying out the integration defined in Eq. (18). The $B(EL)$ and R_{tr} so determined are listed in Table II. It may be noted that Eq. (18) implies that R_{tr} is fixed, once the parameters c_{tr} and t_{tr} are chosen. Thus, in the hydrodynamical model used for present interpretation of the data, all transitions of a given multipole order in a given nucleus will have the same R_{tr}. A more general interpretation of the data is given in Sec. VI C.

In order to facilitate comparison with other data, we have also listed in Table II the radiation transition probabilities in terms of single-particle units and in terms of deformation parameters β_L. The single-particle units are computed as[16]

$$B(EL, 0^+ \to L)_{sp} = [(2L+1)/4\pi][3R_0^L/(3+L)]^2, \quad (22)$$

where

$$R_0 = 1.20A^{1/3}\ \text{F}.$$

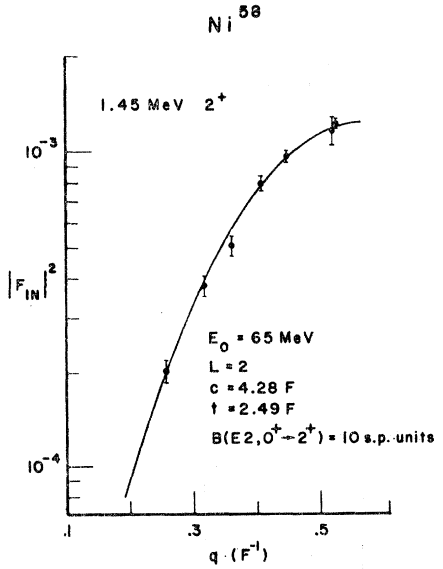

FIG. 19. The theoretical and experimental $|F_{in}|^2$ versus q for the Ni^{58} 1.45-MeV 2^+ state. The solid curve is the $|F_{in}|^2$ calculated by Code GBROW using the strict hydrodynamic model ($c_{tr}=c$; $t_{tr}=t$). The best fit to the data is obtained by a least-squares analysis.

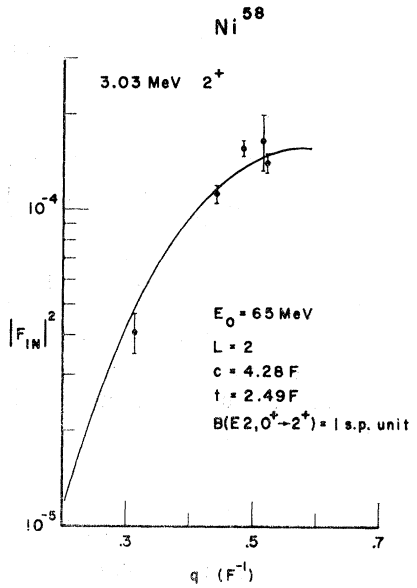

FIG. 20. The theoretical and experimental $|F_{in}|^2$ versus q for the Ni^{58} 3.03-MeV 2^+ state. The solid curve is the $|F_{in}|^2$ calculated by Code GBROW using the strict hydrodynamic model ($c_{tr}=c$; $t_{tr}=t$). The best fit to the data is obtained by a least-squares analysis.

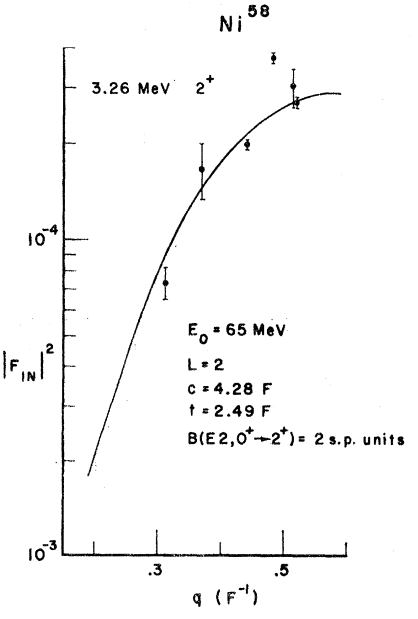

FIG. 21. The theoretical and experimental $|F_{in}|^2$ versus q for the Ni^{58} 3.26-MeV 2^+ state. The solid curve is the $|F_{in}|^2$ calculated by code GBROW using the strict hydrodynamic model ($c_{tr}=c$; $t_{tr}=t$). The best fit to the data is obtained by a least-squares analysis.

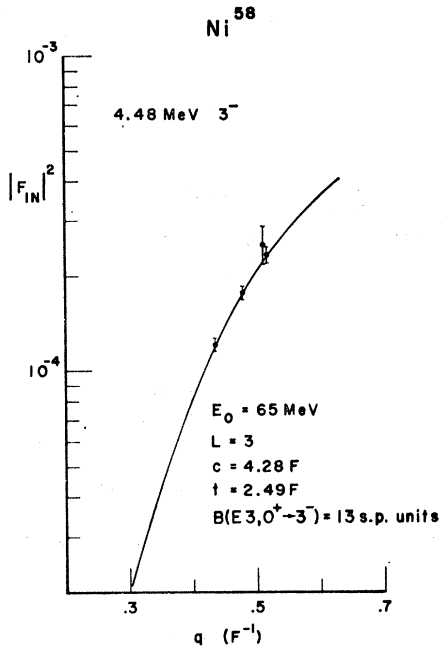

FIG. 22. The theoretical and experimental $|F_{in}|^2$ versus q for the Ni^{58} 4.48-MeV 3^- state. The solid curve is the $|F_{in}|^2$ calculated by Code GBROW using the strict hydrodynamic model ($c_{tr}=c$; $t_{tr}=t$). The best fit to the data is obtained by a least-squares analysis.

These values afford an estimate of the "collectivity" of the transition; for numbers of the order of 1 or smaller, the validity of the hydrodynamical model used in obtaining them is doubtful. The deformation parameters β_L, which measure the amplitude of vibration about a spherical equilibrium shape, are useful for comparison with direct-interaction heavy-particle inelastic-scattering measurements. They are computed in the hydrodynamical model used here as[58]

$$B(EL, 0^+ \rightarrow L) = [(3/4\pi)ZeR_0{}^L]^2\beta_L{}^2. \quad (23)$$

The q dependence of the measured form factors is seen to be consistent with that expected for the levels of known spin and parity, namely, all observed levels except the 3.034- and 3.260-MeV levels in Ni^{58}. For these levels a 2^+ assignment is suggested in Refs. 50 and 51. The q dependence of a longitudinal quadrupole transition is very similar to that expected for a monopole transition; however, a 0^+ assignment for these states is eliminated by observation of a γ-ray transition to the 0^+ ground state.[51] Therefore, the plots in Figs. 20 and 21 confirm the 2^+ assignment.

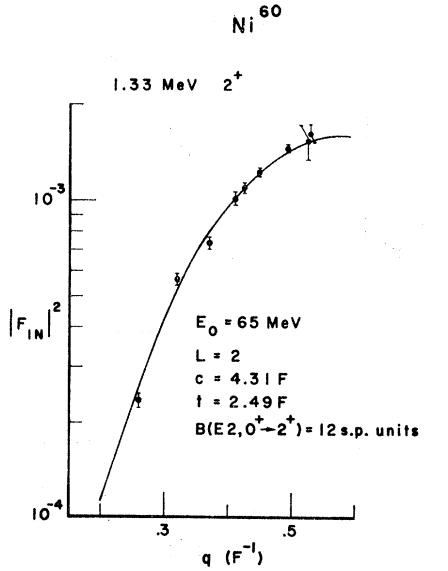

FIG. 23. The theoretical and experimental $|F_{in}|^2$ versus q for the Ni^{60} 1.33-MeV 2^+ state. The solid curve is the $|F_{in}|^2$ calculated by Code GBROW using the strict hydrodynamic model ($c_{tr}=c$; $t_{tr}=t$). The best fit to the data is obtained by a least-squares analysis.

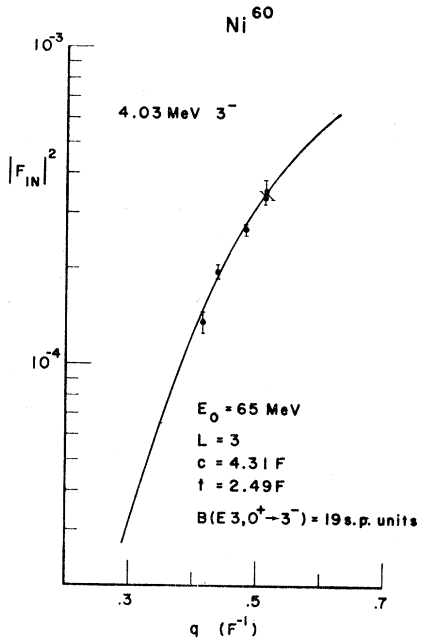

FIG. 24. The theoretical and experimental $|F_{in}|^2$ versus q for the Ni^{60} 4.03-MeV 3^- state. The solid curve is the $|F_{in}|^2$ calculated by Code GBROW using the strict hydrodynamic model ($c_{tr}=c$; $t_{tr}=t$). The best fit to the data is obtained by a least-squares analysis.

VI. DISCUSSION

A. Comparison with Other Measurements

In a preliminary report[18] of the results for the first excited states of these Ni isotopes, we have pointed out that the agreement of the present data with the $B(E2)$ extracted from resonance-fluorescence[59] and Coulomb-excitation[19] experiments is excellent. The comparison

[58] O. Nathan and S. G. Nilsson, in *Alpha-Beta- and Gamma-ray Spectroscopy*, edited by Kai Siegbahn (North-Holland Publishing Company, Amsterdam, 1965), Chap. X.

[59] F. R. Metzger, Phys. Rev. 103, 983 (1956).

TABLE III. Reduced radiative transition probabilities, $B(EL,0^+ \rightarrow L)$ (e^2F^{2L}).

	Level	Coulomb excitation[a]	Resonance fluorescence[b]	Heavy-particle scattering	Electron scattering Ref. 6	Present results
			*E*2 Transitions[c]			
Ni^{58}	1.452 MeV	720±70	...	920 to 1200[d] 535 to 750[e]	990±130	657± 11
	3.034 MeV	...	...	...	} 310± 70	83± 3
	3.260 MeV	...	...	...		153± 15
Ni^{60}	1.330 MeV	910±80	880±160	1360 to 1960[d] 785 to 1200[f]	1250± 150 ...	845± 9
Ni^{62}	1.172 MeV	830±80	...	1200 to 2040[d] 1120 to 1250[g]	...	877± 11
			*E*3 Transitions[c]			
Ni^{58}	4.480 MeV	...	...	14 600 to 16 300[d]	27 000± 3800	18 600±520
Ni^{60}	4.038 MeV	...	...	19 100 to 23 000[d]	35 000± 5600	28 100±640
Ni^{62}	3.75 MeV	...	...	20 600 to 29 800[d] 16 540 to 19 870[g]	...	20 100±540

[a] See Ref. 19.
[b] See Ref. 59.
[c] The errors quoted for $B(EL)$ assume the liquid-drop model for the transition charge density and are purely statistical in nature. The estimate of error from dependence on the parameters of this charge density are ±15% for both $B(EL)$ and R_{tr}. See text.
[d] See Ref. 61.
[e] See Ref. 62.
[f] See Ref. 63.
[g] See Ref. 64.

is restated in Table III. Such "photon experiments" carry the same nuclear information as do electron-scattering measurements at very low momentum transfer; the agreement between these two types of data may be taken as a demonstration by experiment of the validity of Code GBROW.[17] Because of the use of slightly different parameters for the ground-state charge distribution, as well as an improved energy calibration in the present interpretation, the values cited for $B(E2)$ and R_{tr} in Table III differ slightly from preliminary results given in Ref. 18; the changes however, lie within the quoted errors.

In an early inelastic-scattering experiment, Crannell *et al.*[6] have used 183-MeV electrons to study inelastic scattering from Ni^{58} and Ni^{60} in the momentum-transfer range 0.6–0.9 F^{-1}. To afford a direct comparison, the present data were renormalized to 183 MeV using

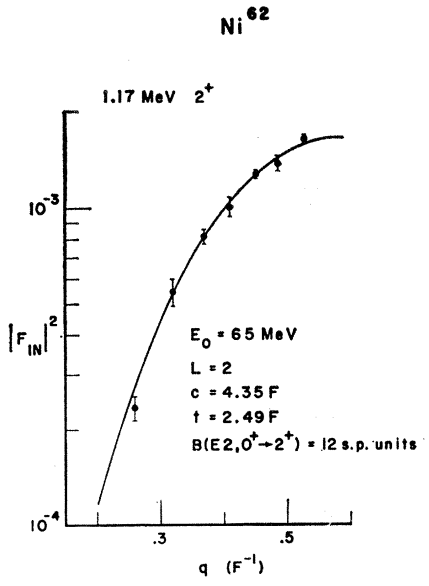

FIG. 25. The theoretical and experimental $|F_{in}|^2$ versus q for the Ni^{62} 1.17-MeV 2^+ state. The solid curve is the $|F_{in}|^2$ calculated by Code GBROW using the strict hydrodynamic model ($c_{tr}=c$; $t_{tr}=t$). The best fit to the data is obtained by a least-squares analysis.

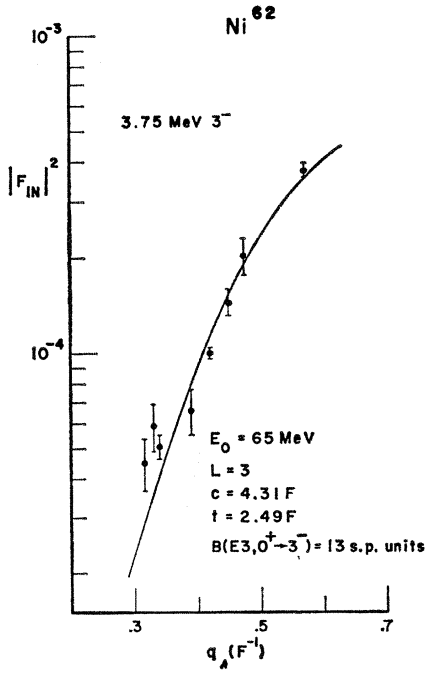

FIG. 26. The theoretical and experimental $|F_{in}|^2$ versus q for the Ni^{62} 3.75-MeV 3^- state. The solid curve is the $|F_{in}|^2$ calculated by Code GBROW using the strict hydrodynamic model ($c_{tr}=c$; $t_{tr}=t$). The best fit to the data is obtained by a least-squares analysis.

Code GBROW. Although the ranges of q do not overlap, it is clear that the present data for the 2^+ state are lower by a factor of about 2. The comparison for the 1.45-MeV 2^+ state and the 4.48-MeV 3^- state in Ni^{58} yields a similar conclusion. The disagreement is partly reflected in the comparison of $B(EL)$ given in Table III. The results of Ref. 6 were derived in the Born approximation, using a transition-charge density of shape similar to that used here. When recomputed using the distorted-wave formalism, Onley, Reynolds, and Wright[17] show that the differences in the $B(EL)$ are worsened, particularly in the $E2$ case. However, the authors of Ref. 6 mention the possibility of a systematic error as large as a factor of 2 in the extraction of their form factors. Recent work may have resolved the disagreement.[60]

Comparison of the present results with data from heavy-particle scattering[61–64] is also stated in Table III. The values of radiative transition probabilities were obtained from the β_L cited in the literature via Eq. (23). In these references, the conventional statistical errors in β_L are not given; rather a range of β_L is stated, corresponding to ranges of uncertainty in the parameters and in the description of the direct-interaction mechanism used in deriving the β_L. It is seen that the range of values obtained in the heavy-particle experiments is rather large, though for the octupole states errors in the present results are larger than the range of β_L quoted. In any case, the worst discrepancy between the heavy-particle results and the electron-scattering results is contained in a factor of 2.

B. Comparison with Sum Rules

Without attempting detailed comparison of our results with theories of the structure of the Ni isotopes, it is of general interest to express the strengths of the transitions relative to two sum rules. The first, based on the shell model, takes the form[65]

$$\sum_f B(EL, i\to f)=(2L+1)Ze^2\langle r^{2L}\rangle/4\pi, \quad (24)$$

where the sum extends over states of all energies up to the meson threshold, and $\langle r^{2L}\rangle$ is the $2L$ th radial moment of the ground-state charge distribution. The other sum rule is the energy-weighted sum rule (EWSR); for excitations with $T=0$ it is[58]

$$\sum_f (E_f-E_i)B(EL, i\to f) = Z^2e^2L(2L+1)^2\langle r^{2L-2}\rangle/8\pi AM. \quad (25)$$

This sum rule does not depend on any model except insofar as it assumes that there are no velocity-dependent forces in the nuclear Hamiltonian.

TABLE IV. Sum-rule limits.

	Level (MeV)	$B(E2,0^+\to 2^+)$ e^2F^4	$\frac{B(E2,0^+\to 2^+)}{\text{SMSR}}$	$\frac{B(E2,0^+\to 2^+)}{\text{EWSR}}$
		$E2$ Transitions[a]		
Ni^{58}	1.452	657 ± 11	0.18	0.05
	3.035	83 ± 3	0.02	0.01
	3.260	153 ± 15	0.04	0.02
			sum 0.24	0.08
Ni^{60}	1.332	845 ± 9	0.22	0.07
Ni^{62}	1.172	877 ± 11	0.22	0.06
		$E3$ Transitions		
	Level (MeV)	$B(E3,0^+\to 3^-)$	$\frac{B(E3,0^+\to 3^-)}{\text{SMSR}}$	$\frac{B(E3,0^+\to 3^-)}{\text{EWSR}}$
Ni^{58}	4.480	18 600 ± 520	0.13	0.08
Ni^{60}	4.038	28 100 ± 640	0.18	0.10
Ni^{62}	3.75	20 100 ± 540	0.13	0.07

[a] The errors quoted for $B(EL)$ assume the liquid-drop model for the transition charge density and are purely statistical in nature. The estimate of error from dependence on the parameters of this charge density are ±15% for both $B(EL)$ and R_{tr}. See text.

The fractions of the sum rules exhausted by the states observed are entered in Table IV. The sum rules were evaluated by calculating $\langle r^n\rangle$ using the ground-state Fermi distributions. It is interesting to note that both the first quadrupole and octupole states exhaust about 20% of the shell-model sum rule, which constitutes another statement of their highly collective nature. (This is in contradiction to the statement in Ref. 6 that the shell-model sum rule is exceeded by the first excited state of Ni^{58} and Ni^{60}; it seems that an error was made in computation of this limit.) The fact that the observed states exhaust only 10% of the EWSR is an indication that other quadrupole and octupole excitations must exist at higher energies, as suggested by the results quoted in Ref. 66.

C. Model Independence

The distorted-wave analysis requires the assumption of a specific transition charge density, that is, it requires a model for the nuclear charge distribution. In the foregoing analysis, a hydrodynamical model has been employed. This circumstance raises the question of whether the values of $B(EL)$ and R_{tr} have any validity beyond the confines of the model assumed. On the other hand, matrix elements derived from measurements at low momentum transfer are not expected to be very sensitive to the model; contributions to the form factor (Eq. 10) from the nuclear interior are strongly suppressed by the behavior of the spherical Bessel function for small qr.

In an empirical attempt to determine how closely the experimental data define the parameters of the transition charge density, distorted-wave calculations were performed for values of c_{tr} and t_{tr} which varied as much as ±50% about the values $c=4.31$ F and $t=2.49$ F

[60] M. R. Yearian (private communication).
[61] S. F. Eccles, H. F. Lutz, and V. A. Madsen, Phys. Rev. **141**, 1067 (1966).
[62] H. W. Broek, J. L. Yntema, B. Buck, and G. R. Satchler, Nucl. Phys. **64**, 259 (1965).
[63] J. K. Dickens, F. G. Perey, and G. R. Satchler, Nucl. Phys. **73**, 529 (1965), references quoted therein.
[64] A. L. McCarthy and G. M. Crawley, Phys. Rev. **150**, 935 (1966).
[65] A. M. Lane and E. D. Pendlebury, Nucl. Phys. **15**, 39 (1960).
[66] R. Ballini, N. Cindro, J. Delaunay, J. Fouan, M. Loret, and J. P. Passerieux, Phys. Letters **21**, 708 (1966).

describing the (fixed) ground state of Ni^{60}. The results of these calculations compared to the data for the first excited state of Ni^{58} are shown in Fig. 27. Numerical values of χ^2/N obtained in fitting the theoretical curves to the data are plotted for each pair of values (c_{tr},t_{tr}) for which the calculations were made. It is seen that the values of these parameters for which $\chi^2/N<2$ lie within the indicated contour, and that all other values lie outside. This contour is taken as a measure of the degree to which the experimental data fix the parameters for model transition charge densities of the form of Eq. (20). It is seen that there exists a family of acceptable parameter pairs (c_{tr},t_{tr}); each of these pairs are consistent with the measured form factors.

With each value of (c_{tr},t_{tr}) there are associated a set of moments of the charge distribution, notably $B(E2)$ and R_{tr}^2, as given in Eqs. (16) and 1(8). In Fig. 28, results of the same calculations shown in Fig. 27 are replotted against $B(E2)$ and R_{tr}^2. Again the values of χ^2/N representing the quality of fit are indicated; but here the criterion $\chi^2\leq 2$ isolates a set of values $B(E2)$ and R_{tr}^2. We have taken this plot (and similar ones for the first 2^+ states of Ni^{60} and Ni^{62}) as establishing the accuracy with which we have measured a "parameter-independent" $B(E2)$ and R_{tr}. The results quoted in Table II lie within such contours, but it is clear the errors of $\pm 15\%$ on the parameter-independent values of $B(E2)$ and R_{tr} are considerably larger than the errors given in Tables II–IV.

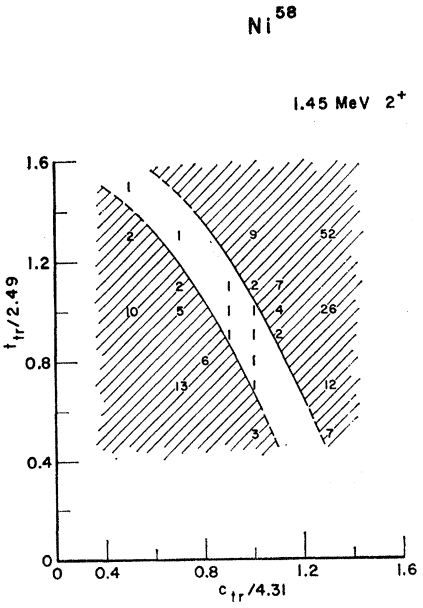

FIG. 27. Plot showing the results of the computer-fitting experiment. The data shown in Fig. 19 were least-squares fitted to GBROW $|F_{in}|^2$ curves for different values of c_{tr} and t_{tr} while leaving the ground-state parameters fixed. At each point (c_{tr},t_{tr}) the value of the resulting χ^2/N is entered. All fits with $\chi^2/N<2$ are considered equally good and are shown in the unshaded contour. A family of (c_{tr},t_{tr}) pairs is thus defined, all of which give equally good fits to the data. See the text.

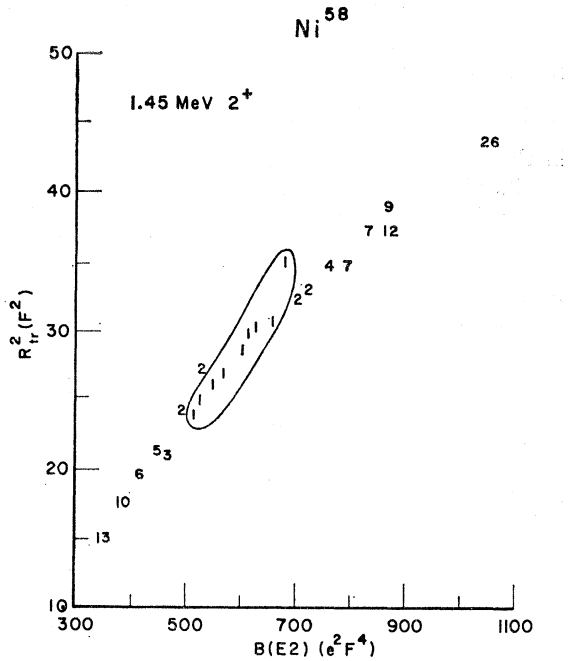

FIG. 28. The results of the same calculations as for Fig. 27 are replotted in terms of $B(EL)$ and R_{tr}^2. The countour enclosing all $\chi^2/N<2$ is shown. The limits of the contour isolate a set of values of $B(E2)$ and R_{tr}^2. See the text.

Pursuing further the question of the degree of determination of the transition charge distributions by the data, the $L+4$ moments of the charge distributions were calculated. A χ^2/N plot for values of $B(EL)$ versus I_{L+4}/I_L, the third term in Eq. (13), showed a considerably wider spread than does Fig. 28. We conclude that the data may be considered to fix pairs of values $B(E2)$ and R_{tr}^2 with fair accuracy but that higher moments are not well determined in the low-q range explored here.

The quality of the data for levels other than the first 2^+ states is insufficient to permit significant study of parameter variation. The $B(EL)$ and R_{tr} quoted in Tables II–IV were obtained assuming radius and skin-thickness parameters for the transition charge density equal to those for the ground state. This equality is equivalent to assumption of the strict hydrodynamical model. The errors quoted in Table II–IV are likewise appropriate only within the hydrodynamical model.

It should be emphasized that our values of $B(E2)$ and R_{tr}^2 cannot be claimed to be model-independent. Our use of the distorted-wave formalism in its present form requires the assumption of a specific form for the transition charge density; we have used only the form of Eq. (20). Our values of $B(E2)$ and R_{tr} are not independent, as indicated by the clustering of computed values in Fig. 28 about a rather well-defined curve. Thus we can claim to have investigated only "parameter independence" rather than model independence in the broadest sense. While the $B(E2)$ is expected to be

model-independent, the sensitivity of R_{tr}^2 to the model assumed remains to be ascertained.

VII. CONCLUSIONS

In addition to producing specific data relevant to nuclear models of the Ni isotopes, we believe that the present study demonstrates the value of inelastic electron scattering at energies below 100 MeV in obtaining moments of charge distributions involved in transitions from the ground state. The availability of variable-energy electron beams with energies known to the order of 0.05% and energy spreads of the order of 100 keV is a significant development; though limited in momentum-transfer capability, such beams open for exploration a significantly larger manifold of individual nuclear states that has been available with higher energy beams which have correspondingly larger energy spreads. Coincidental with this technical progress, the development of the distorted-wave code GBROW by the Duke group has made it possible to test theoretical transition charges and current densities against such data, and hopefully, to extract certain moments of the charge distributions which are not strongly model-dependent. The L th moment, the $B(EL, i \rightarrow f)$ of Eq. (15) is well known; the $L+2$ moment [the R_{tr}^2 of Eq. (18)] deserves wider attention than it has heretofore received.

In the strict hydrodynamical model, the form for ρ_{tr} given in Eq. (20) can be inserted into the definition Eq. (18). The integration can be carried out, yielding

$$R_{tr}^2=\frac{2L+3}{2L+1}\left[\frac{\int_0^\infty r^{2L+2}\rho_{g.s.}(r)dr}{\int_0^\infty r^{2L}\rho_{g.s.}dr}\right]$$
$$=\frac{2L+3}{2L+1}\frac{I_{2L}}{I_{2L-2}}\bigg|_{g.s.}=\frac{2L+3}{2L+1}\frac{\langle r^{2L}\rangle_{g.s.}}{\langle r^{2L-2}\rangle_{g.s.}},$$

where "g.s." indicates ground state. Since our data can be fitted by this model, they satisfy this relation.

The Darmstadt group early recognized the possibility of extracting such information from electron scattering below 100 MeV. As presented by Spamer,[9] Fig. 29 shows values of reduced transition radii $R_{tr}/A^{1/3}$ as a function of mass number. Values from the present work are added. It is seen that values of the reduced transition radii for quadrupole and octupole transitions are relatively constant and appear to be somewhat larger than those for $M1$ transitions.

The reduced transition radii are just slightly larger than the reduced half-density radius of the ground states; this is consistent with the generalization that inelastic-scattering experiments at low momentum transfer are sensitive primarily to effects of the nuclear surface. We believe that theoretical consideration of the transition radii will afford valuable insights on the outer portions of nuclear charge distributions.

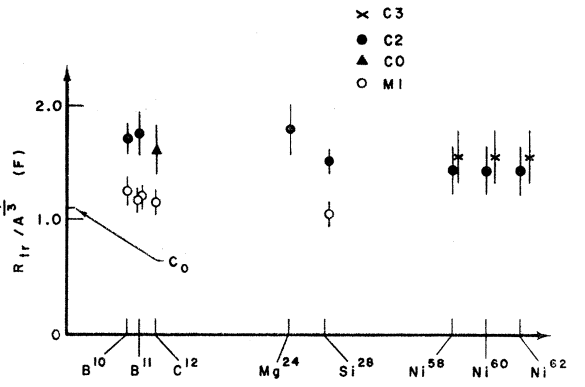

FIG. 29. The reduced transition radii for many different transitions in different nuclei are compared. The data on light nuclei were taken from Ref. 9. The arrow marks the value of $c_0(=c/A^{1/3})$ used in the data analysis.

ACKNOWLEDGMENTS

Professor Gerald A. Peterson was primarily responsible for the initial assembly of the electron-scattering system; Edmond Comeau gave generously of his time and talent in its construction, alignment, and maintenance. We are indebted to members of the experimental group at Darmstadt for generous sharing of their experiences. Dr. L. E. Wright and Shiang-tai Tuan of Duke University, and Dr. D. Onley and Ohio University together with Dr. James Ziegler provided the distorted-wave code and many valuable comments. David Madsen and William Metz helped in obtaining the data and in the energy calibration. Charles Gingell directed the construction of most of the circuits used. Joseph Berti and Albert Nelson designed many of the parts used in the experiment, and Albert Comeau and Joseph Cimino constructed them. We are particularly indebted to Phillip Jewett, Walter Knudsen, Sidney Clow, Roy Rondoe, Marvin Garfield, and Frank Hegedus, who provided a reliable and stable accelerator beam. Finally, we thank Professor Howard Schultz for his constant interest in this study, and for his labors in administration which have provided the stimulating environment in which we work.